Three-dimensional PIV measurements of bubble drag and lift coefficients in restricted media

J. Ortiz-Villafuerte
Departamento de Sistemas Nucleares, Instituto Nacional de Investigaciones Nucleares, Carretera México-Toluca s/n, La Marquesa, Ocoyoacac, Estado de México, MÉXICO 52750.
e-mail: javier.ortiz@inin.gob.mx

W. D. Schmidl and Y. A. Hassan
Department of Nuclear Engineering, Texas A&M University, College Station, Texas, USA 77843-3133,
e-mail: dschmidl@gmail.com; y-hassan@tamu.edu

Received 24 May 2012; accepted 23 May 2013

A hybrid scheme combining Particle Image Velocimetry and Shadow Image Velocimetry has been used for a full-volume, three-dimensional, transient study of the shape, trajectory and forces acting on air bubbles rising in stagnant tap water in restricted media. The bubble Reynolds number ranged from 400 to 650. The three-dimensional reconstruction of the bubble was accomplished by combining images from two orthogonal views. This reconstruction process allowed for measurement of dimensions, orientation, trajectory, rotation, velocity and acceleration of an individual rising bubble. These parameters were then used to compute drag and lift forces acting on the bubble. Instantaneous values of drag and lift coefficients were then determined. These experimental results were compared to known experimental data and values obtained from correlations found in scientific literature. It was found that correlations intended for determining drag coefficient values should be adequately modified when necessary to account for wall impact, since the drag coefficient magnitude is considerably higher than that predicted by such correlations at Re below 550. Regarding the bubble lift coefficient, instantaneous data scatter noticeably as a function of Re, but average values agree within the range of known data.

The major contributors to the uncertainty in this experiment were the capability of accurately reconstructing the 2D shape of the bubbles from distorted and/or incomplete PIV images and determining the bubble centroid. An overall error of 7% was computed for the drag coefficient, but it rises up to 44% for the lift coefficient.

Keywords: PIV; bubble; lift; drag; coefficient.

PACS: 47.55.dd

1. Introduction

The interaction between continuous and dispersed phases in a bubbly flow is a phenomenon not completely understood that still needs to be studied. Bubbly flow is an important regime in the nuclear, chemical, petroleum, and medical industries, among others. Most two-phase bubbly flow systems employed in industry consist of bubbles rising in swarms. However, considering the dynamics of a single bubble and its associated wake can provide a first approach to understand the complex interaction phenomena between bubbles and wakes. Dilute bubbly flows are an extension of single bubble dynamics. Therefore, any improvement in the description and modeling of individual bubble motion, flow field around a bubble, and dynamical interactions between bubble and flow will ultimately improve bubbly flow modeling. This is because many of the assumptions for modeling two-phase flow are directly related to phenomena involving single bubbles. Frequently, drag, added mass, and lift coefficients used in bubbly flow analysis are measured or computed for single bubbles.

An important aspect of bubbly flow dynamics is bubble movement in restricted media. One particular example where this kind of flow occurs is in fuel assemblies of light water reactors. In the nuclear power industry, fuel assembly designs have evolved, in part, by increasing the number of fuel rods in an assembly. Thus, the heat transfer area has increased, while lowering the linear heat generation rate value. In old, typical boiling water reactor 8×8 fuel assemblies, the equivalent diameter of an interior subchannel was about 13.5 mm, while in modern 10×10 designs the same parameter is about 10.4 mm; a decrease of about 23%. This dimension decrease has an impact on drag and lift coefficients of rising bubbles, but it is not always taken into account for bubbly flow modeling.

Particle dynamics in flows have been studied previously, and several reviews have been published on this subject [1,2]. Among the first detailed experimental studies on rising bubbles in liquids was performed by Haberman and Morton [3], and it is still an important source of data. However, questions about the response of particles to turbulent and vortex-type flows or the interactions of particles with wall turbulence are still being investigated [4]. Since the forces experienced by the particles determine their response to the surrounding ambient conditions, the equation of motion of particles should incorporate all the forces affecting the particle dynamics. However, the unsteady nature of some forces and their appropriate formulation makes it difficult to solve for all the instantaneous forces acting on the particle [5].

Measurements of drag and lift forces are generally performed for $\mathrm{Re}_p > 100$ [6]. In this study, the Re number was in the intermediate range (400 to 650) for air bubbles rising in tap, stagnant water in a 12.7 mm diameter circular pipe.

Thus, wall influence on bubble motion was an important parameter to consider when determining drag and lift coefficients. The Particle Tracking Velocimetry (low density mode of the Particle Image Velocimetry technique) and the Shadow Image Velocimetry technique are combined together to measure the liquid velocity field and bubble dimensions, trajectories, and velocities, and from those, the drag and lift forces acting on a bubble. An error analysis was performed to determine the accuracy of the measurements. Also, a comparison of values of drag and lift coefficients against data found in literature is presented.

2. Bubble motion equation and nature of forces acting on a bubble

The trajectory of a particle is computed by integrating its momentum equation. Starting from the Basset-Boussinesq-Oseen equation with correction factors to account for Reynolds number and acceleration effects [7], the equation of motion for a freely rising bubble in a uniform flow becomes,

$$V_b\,\rho_l\left[\frac{\rho_b}{\rho_l}\frac{d\,\mathbf{v}}{d\,t}+C_{\mathrm{M}}\left(\frac{d\,\mathbf{v}}{d\,t}-\frac{d\,\mathbf{u}}{d\,t}\right)-\frac{D\,\mathbf{u}}{D\,t}\right] = V_b(\rho_b-\rho_l)\mathbf{g}+\left[\frac{1}{2}C_D\rho_l A_b \parallel \mathbf{U_r} \parallel \mathbf{U_r}\right]_{\Uparrow} + \left[\frac{1}{2}C_L\,\rho_l\,A_b \parallel \mathbf{U_r} \parallel \mathbf{U_r}\right]_{\perp} \quad (1)$$

where the subscripts b and l are associated to the bubble and liquid, respectively, $\mathbf{v}$ is the bubble velocity vector, and $\mathbf{u}$ is the liquid velocity vector. The coefficients C_M, C_D, and C_L, are the added mass, drag and lift coefficients, respectively. V and A are the volume and projected area of the bubble, ρ the density, $\mathbf{g}$ is the gravity vector, and U_r the relative velocity between the two phases, which is given by

$$\mathbf{U_r} = \mathbf{v} - \mathbf{u}. \quad (2)$$

The Faxen and Basset forces are not included in (1) because they are not relevant for bubbles in quiescent liquids [8]. The left hand side of (1) represents the total inertia of the system. On the right hand side, the expressions for buoyancy, drag, and lift forces are shown. The formulation for the lift force is a common one used in aerodynamics for the total lift. This form of the drag and lift forces allows for a simpler calculation of the drag and lift coefficients. The parallel ($\Uparrow$) and perpendicular ($\perp$) symbols at the right side of the brackets are introduced to denote that the drag force acts parallel to $\mathbf{U}_r$, while the lift is normal to it. The substantial acceleration of the liquid, the relative velocity and the cross product in the original formulation of the lift force are all evaluated at the center of the bubble (as if the bubble was not there).

The buoyancy force is due to the density difference between bubble and liquid. The virtual or mass force, included in the inertia term of (1), is an unsteady force due to acceleration of the relative velocity between bubble and liquid. It is the force needed to accelerate the liquid surrounding the bubble. The liquid acceleration comes from the work done by the bubble on the liquid. The added mass coefficient C_M has a value of 0.5 for spherical particles, according to potential flow theory. However, C_M is actually a tensor called the added mass matrix, or induced inertia tensor [9]. The drag force is a well studied force on many kinds of fluid and solid particles. The drag coefficient C_D is commonly calculated through empirical correlations, which only depend on Re. However, these correlations yield average values, which can notoriously deviate from instantaneous values, due to unsteadiness of the flow, variation of the projected area, and/or particle acceleration. The average C_D is usually determined through the expression for the drag force in (1) assuming that the particle already travels at terminal velocity and no lateral forces are present. Consequently, the drag force balances the buoyancy force. Results have shown that depending on the average estimate used to analyze the experimental data, C_D values can be considerably different [10]. Another problem regarding C_D is the contamination of the system in which fluid particle moves.

In bubbly flows, the phenomenon of phase distribution has been associated with the turbulent structure in the liquid phase, and with the lift force acting on the bubble. The lift force plays a key role in bubble migration, and then phase distribution, because it is normal to the direction of the particle motion. The lift force arises due to vorticity generation at a rigid surface, and bubbles moving in contaminated liquids have a behavior similar to rigid particles. The vorticity can also be generated due to shear in the liquid. Because of the vorticity field surrounding the bubble, an uneven pressure distribution yields a lateral force which may induce lateral movement of the bubble. For large Re, C_L = 0.5. This is obtained from potential inviscid flow and it is widely used. The same value can also be used in an accelerated flow [11]. Purity of the continuous phase is also important when determining the lift coefficient. For $\mathrm{Re}_p > 35$, Takamura and Magnaudet [12] found out that the lift force on contaminated bubbles was directed away from the wall, while on clean bubbles the lift force was directed towards the wall. Taking into consideration the complex phenomena involved in bubble motion, it is clear that performing accurate measurements of the drag and lift coefficients is important for engineering applications and a challenge too, since both steady and unsteady forces are difficult to be accurately predicted in contaminated systems at relevant Re [8].

3. Measurement technique and experimental set-up

In this experimental study, both continuous and dispersed flow fields were measured simultaneously, although only bubble motion data are relevant for the measurement of drag

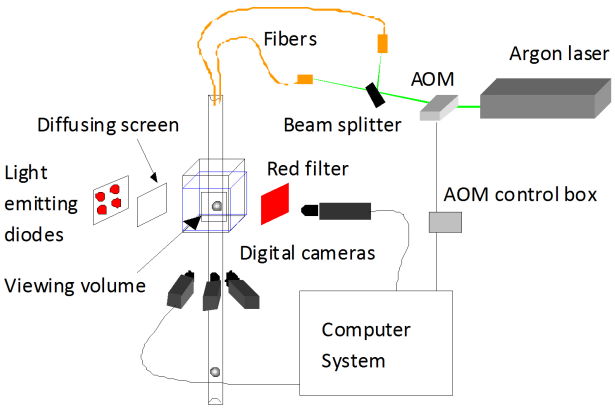

FIGURE 1. Facility set-up.

and lift coefficients, because there was no liquid flow. The measurement technique employed herein is a hybrid technique to identify the bubble shape and the velocity fields of both the liquid and the bubble. The three-dimensional (3D) liquid velocity field was obtained via a stereoscopic Particle Tracking Velocimetry (PTV) technique, while the 3D bubbles' shape and velocity vector were determined with image data from a Shadow Image Velocimetry (SIV) technique and standard Particle Image Velocimetry (PIV) pictures.

The experimental set-up consisted of a flow system, an optical system and a data acquisition system. A schematic of the experimental set-up is shown in Fig. 1. Air bubbles of about 3-mm spherical-equivalent diameter were injected into a 12.7-mm i.d., 15.9-mm o.d., 1.3-m long Plexiglas pipe. The flow was seeded with polystyrene tracer particles. The density of these particles was 1.05 g/cm^3 and their diameter was 40 μm. The measurements were carried out at a location of about L/D = 66, where L is the length from pipe inlet to measurement zone, and D is the pipe inner diameter. A water filter removed any contaminants larger than 5 μm prior to the addition of the tracer particles. Enclosing the test section in a rectangular Plexiglas box filled with water reduced the pipe curvature effect. The Plexiglas box has the same refractive index as that of the pipe.

For the PTV measurements, the optical elements of the set-up included an argon ion laser, an acoustic optic modulator (AOM), a beam splitter, mirrors, and a multimode fiber with a fiber coupler. The light source was the argon ion laser. The 514-nm frequency was selected for illumination. The laser beam passed through the AOM, which chopped the continuous laser light at intervals of 16.67 ms. The laser pulse width was 250 μs and the AOM or Bragg Cell has a rise time less than 200 ns, so it has no impact on the strength of the beam reaching the viewing volume. The light beam was transmitted to the viewing volume through two 400-μm multimode fibers. These two fibers were placed at the top of the tube to illuminate the viewing volume with cones of light. Note that creating a thin sheet of light, as normally done in PIV measurements would not cover the whole test volume, and thus it would have been quite difficult to performed full-volume measurements of the liquid velocity field, and accurately follow the bubble path. The quality of images (size, intensity and distribution of particles) indicated that the laser beams adequately illuminated the viewing volume. The image-data were stored on imaging boards (frame grabbers) installed in personal computers. These imaging boards also had the function of controlling the signals required to synchronize the AOM and the Charged Couple Device (CCD) camera triggering.

Four CCDs 640×480-pixel cameras were used; three of which were employed for the PTV liquid velocity field measurements. Additional optical elements were attached to the CCD cameras to improve the accuracy of the measurements. These elements included close-up and telephoto lenses, extension rings and (light) intensifier tubes. As referenced in Fig. 1, the three PIV cameras are denoted from now on as L (Left), C (Center), and R (Right). To measure bubble dimensions, the PIV system was supplemented with the SIV method, which in this work is a red shadow image technique [13,14]. As also shown in Fig. 1, a red filter was placed in front of the camera that was set perpendicular, and on the same plane, to the C camera. That camera is referred to as S (Shadow) camera from now on. The filter blocked the laser green light and only allowed red light to pass through. The shadow is produced by the reflected red light rays from light emitting diodes (LEDs), located opposite to the S digital camera. All four cameras were run at 60 frames/s (field mode), to take advantage of the higher framing rate, with a resolution of only 640×240 pixels. One of the major advantages of positioning the cameras as shown in Fig. 1 was that the orthogonal cameras (C and S) would provide directly two out of the three world coordinates of the centroids of the seed particles and the bubbles. For the liquid velocity field measurement, the L and R cameras provided information for estimating the out of plane coordinate (y), via the stereoscopic viewing technique.

3.1. Camera calibration

Camera calibration is the technique to determine the camera parameters, using a set of image points with known world coordinates. More than 500 image calibration points and corresponding world coordinate were registered for the calibration process. Camera parameters include camera position in the world coordinate system and orientation, and also internal parameters, such as focal length, or principal point distance, lens distortion parameters, etc. In this study, it was decided that camera calibration was performed *in situ*, using a perspective projection. This is simply a transformation of a 3D world point into a 2D image. The set of equations relating the world coordinates and image coordinates are known as the Direct Linear Transformation method [15].

3.2. Continuous velocity field measurement

Once the PIV data images were recorded, the first step, before starting the particle tracking process to obtain 2D vectors, is to compute the image tracer centroid. In this work, a locally developed, and improved over the years, routine based

on both grey scale and area was used to determine the 2D position of a tracer on the images. Since image spots of both the tracer particle and the bubble appeared simultaneously on the PIV pictures, it was necessary to remove those spots not required for the respective analysis of liquid or air bubble flow fields. The spot removing process was performed by first comparing image spot sizes. Then, tracer particles were matched from one frame to the next with two different techniques: the spring model [16] and the ART2 Neural Network (ART2NN) technique [17]. Once the tracking step was finished with each technique, the 2D vector data are combined and repeated vectors are filtered out.

As discussed before, the combination of data from the camera pairs L-C and R-C allowed for determining the 3D position of tracer particles. Thus, to determine the third (y) coordinate of velocity vectors it was necessary to match the same 2D velocity vector in at least two of the cameras used for the PIV process. To achieve this, a velocity vector obtained from the tracking of image data from the C camera is chosen first. Then the potential matching candidate vectors are identified from the R or L camera vector data. The candidate vectors must satisfy three constrains: a) the difference in the magnitude, in pixels, of the z-world coordinate was less than a given tolerance ε_z; b) the x-image coordinate of the possible match vector was in a bounded range which depended on the y-world coordinate (the depth); and c) finally, the epipolar geometry [18] constraint was applied to every candidate vector.

3.3. Bubble dimensions measurement

Several methods exist to identify and, if necessary, reconstruct object shapes. When the object to be recognized and reconstructed is symmetric, the dynamic generalized Hough transform (DGHT) algorithm [19] has proven to be particularly useful. For an ellipse, for example, the DGHT provides coordinates of the center point, angle of rotation, and value of the two semiaxes. Further, this algorithm can be used when some occlusion of objects appears on the image. Once the parameters of the boundary shape are known from the hybrid approach of PIV and the shadow images, it is necessary to compute these parameters in world coordinates. In this study this was easily accomplished because the C and the S cameras were parallel to the XZ and YZ planes, respectively.

During most of the measurements the bubble could be seen in 3 or 4 frames, but in rare events up to 5 frames captured the bubble image, out of the total 27 images acquired for each bubble release. The 3D reconstruction method was applied to every time step, that is, to those 3, 4 or 5 frames, in which the bubble showed up in the image data. An example of a bubble trajectory close to the wall is shown in Fig. 2.

4. Error analysis

In this experiment, bubbles were released individually in quiescent water. The time interval between each bubble release was a few minutes. This time separation was enough to obtain quiescent flow between successive bubble injections. It took less than a few seconds for the disturbances generated by the bubble to vanish, so the flow was totally stagnant when the next bubble was released. The question of possible influence from the tracer particles, being 5% heavier than water, on the liquid flow field measurements was considered by calculating their particle Stokes number (St), which resulted in St = 5.72×10^{-3}, so the tracers closely followed flow changes, and thus tracer dynamics did not bias the measurements significantly.

For the computation of the bubbles' dimensions, velocity, and their body forces, it is required to determine the error propagation through the different, and sequential, calculations. In this work, the error propagation formula used is:

$$\sigma_s^2 = \left(\frac{\partial s}{\partial r_1}\right)^2 \sigma_{r1}^2 + \left(\frac{\partial s}{\partial r_2}\right)^2 \sigma_{r2}^2 + \left(\frac{\partial s}{\partial r_3}\right)^2 \sigma_{r3}^2 + ..., \quad (3)$$

where σ_s is the total uncertainty associated to a measured quantity s, which depends on the values of the measurements r_1, r_2, and r_3, and their respective associated uncertainties σ_{r1}, σ_{r2}, and σ_{r3}.

First, the uncertainty in the area projected and volume of the bubbles was calculated. As it can be noted in (1), these parameters influence the computation of inertia and body forces. As an example of how (3) was applied, consider the case of the uncertainty associated to the projected area of a bubble. In order to obtain an average uncertainty for all bubble-images, the spherical-equivalent diameter ($d = [6V_b/\pi]^{1/3}$) was used as the independent uncertain variable, instead of using the ellipse axes, since d is very commonly used in bubbly flow calculations. Thus, in this case (3) becomes:

$$\frac{\sigma_A}{\sigma_d} = \frac{\pi}{4}\,(2\,d) \quad (4)$$

Every bubble image, from both orthogonal cameras, was enhanced and then the boundaries were determined visually. This methodology was developed because the bubble PIV images showed only fragments of the bubble, and the tracer spot images also appeared on those images, as it was shown in Fig. 2, so the automated determination of boundary pixels was not as accurate as required. It is clear that SIV images can yield more accurate data. The boundary pixels were then fed into the DGHT algorithm. The values of the semiaxes from the DGHT algorithm were used to construct ellipses, which were then superimposed over the original bubble images. The results showed that the differences in dimensions of any of the reconstructed axes were at most 80 μm. Although it is expected that this maximum error value arises from the x coordinates, which are determined from the PIV images, it was also applied to the other two axes. Note, furthermore, that the bubbles were not perfect ellipsoids, so this is another component of the total uncertainty. Starting with this value of 80 μm, for each axis value and therefore for d

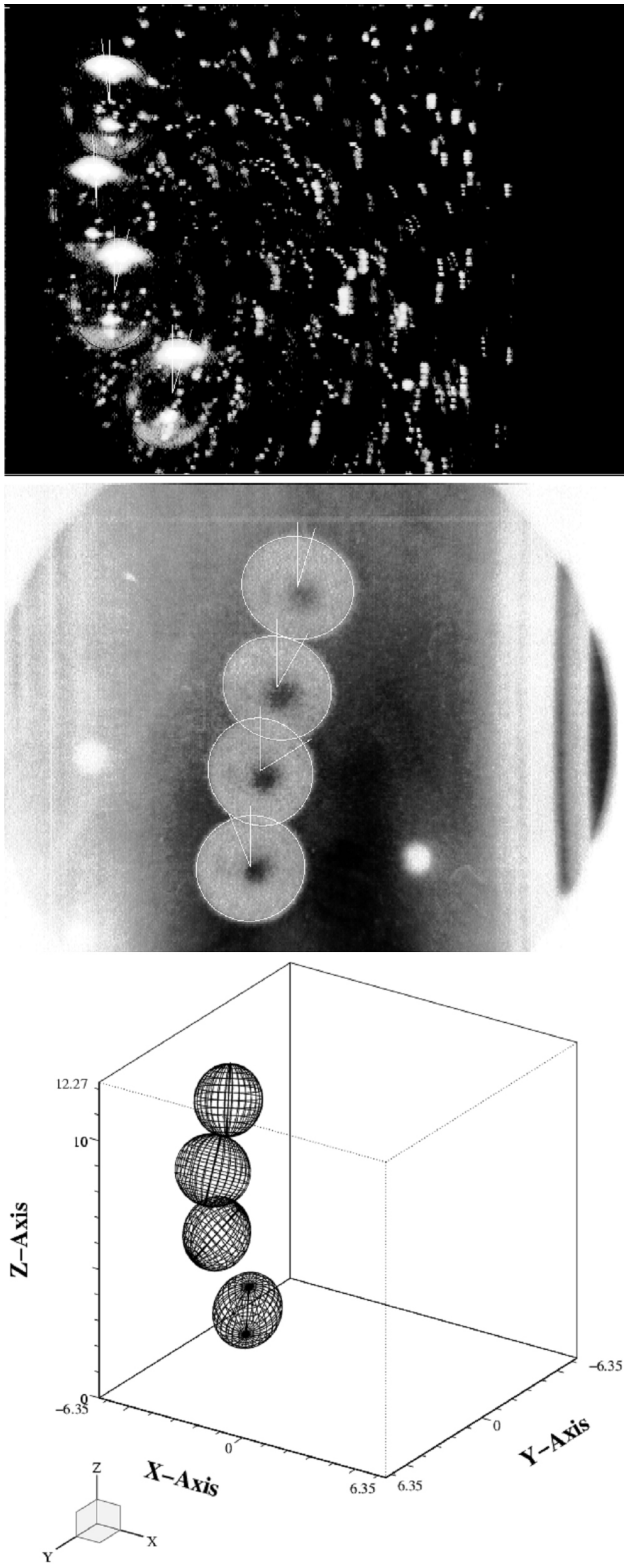

FIGURE 2. Example of a bubble trajectory along the pipe wall. The two-dimensional projections of the bubble on four consecutive frames from the C-S camera pair and the three-dimensional bubble reconstructions are shown.

too, and using the error propagation formula, it can be found that the bubbles' projected area and volume have average uncertainties of about 0.25 mm^2 and 0.5 mm^3, respectively. Such values represent about 4% and 5%, respectively, of the values measured for those parameters via image analysis.

The computation of the drag and lift coefficients require computing the forces acting on the bubble first. To do this, it is necessary to calculate only bubble velocity and acceleration, which have uncertainties derived from errors on locating the bubble image centroid, since in this experiment there was no liquid flow (**u** = **0**). The uncertainty in world coordinates of the centroid of the bubbles was taken directly from the root-mean-squared (rms) error values obtained during camera calibration for each world coordinate, as described in Sec. 3.1. That is, once the image coordinates were known, the calibration data were used to determine the world coordinates of the bubble centroids. These (rounded-off) rms errors were: 0.08 mm in the X direction; 0.03 mm in the Y direction; and 0.03 mm in the Z direction. Then, the uncertainty of, for example, the x-component of bubble velocity can be calculated from, using (3),

$$\sigma_{V_x} = \frac{1}{\Delta t}\sqrt{2\,\sigma_x} \tag{5}$$

Note that no uncertainty is assumed for the framing rate. Thus, the uncertainties for each component of bubble velocity vector were: 6.56 mm/s in the X direction, 2.13 mm/s in the Y direction, and 2.15 mm/s in the Z direction. The acceleration uncertainty σ_a was computed similarly to (5), using the already calculated σ_V. Thus, for each component, the uncertainty values calculated were: 556.70 mm/s^2 in the X direction, 181.36 mm/s^2 in the Y direction, and 182.27 mm/s^2 in the Z direction. Although the range of velocities and accelerations was quite wide, and usually depended on how close the bubbles were to the pipe wall, the uncertainties of velocity components, on average, were 25% in the X direction, 5% in the Y direction, and 3% in the Z direction. For the acceleration components, the uncertainties were on average: 35% in the X direction; 7% in the Y direction; and 4% in the Z direction.

5. Computation procedure of bubble drag and lift coefficients

Once the bubbles' dimensions, velocity and acceleration data were processed, frequently required parameters used in the bubbly flow numerical simulations, such as the drag and lift coefficients, besides the nondimensional numbers associated with the bubble, were computed as shown next. Note that (1) can be represented as follows:

$$\mathbf{F_r} = \mathbf{F_i} - \mathbf{F_g} = \mathbf{F}_\mathrm{D} + \mathbf{F}_\mathrm{L} \tag{6}$$

where $\mathbf{F}_i$ is the total inertia force, $\mathbf{F}_g$ is the buoyancy force, and $\mathbf{F}_D$ and $\mathbf{F}_L$ represent the drag and lift forces, respectively. The required Lagrangian velocities and accelerations for the force calculation were obtained by tracking the bubble motion in at least three consecutive frames, as shown in Fig. 2. Note that the uncertainty of $\mathbf{F}_r$ arises only from the bubbles'

TABLE I. Average values of dimensions, speed, Reynolds number, and drag and lift coefficients of bubbles.

a [mm]	b [mm]	c [mm]	d [mm]	U_b [mm/s]	Re_b	C_D	C_L
1.25	1.45	1.36	2.70	189.79	518.58	0.94	0.39

volume and acceleration, since densities and C_M are considered constant, and $\mathbf{U}_r = \mathbf{v}$. Then, using the average values calculated before, the uncertainties of each component of $\mathbf{F}_r$ were calculated to be: 35% in the X direction; 9% in the Y direction; and 6% in the Z direction. Thus the lift force, and consequently the lift coefficient, will have associated errors larger than those of the drag coefficient, since the lift force is perpendicular to the relative velocity vector.

Then, since $\mathbf{F}_D$ is parallel to the relative velocity $\mathbf{U}_r$, it can be computed from the projection of $\mathbf{F}_r$ in the direction of $\mathbf{U}_r$, that is,

$$\mathbf{F}_{\mathrm{D}} = \frac{\mathbf{F_r} \bullet \mathbf{U_r}}{\|\mathbf{U_r}\|} \frac{\mathbf{U_r}}{\|\mathbf{U_r}\|}. \tag{7}$$

And then lift force components can be calculated from

$$\mathbf{F}_{\mathrm{L}} = \mathbf{F_r} - \mathbf{F}_{\mathrm{D}}. \tag{8}$$

Once the magnitudes of the drag and lift forces are known, the respective coefficients can be computed. For example the drag coefficient is obtained from:

$$C_{\mathrm{D}} = \frac{\|\mathbf{F}_{\mathrm{D}}\|}{\frac{1}{2}\rho_l A_b \|\mathbf{U_r}\|^2}, \tag{9}$$

and similarly for the lift coefficient. Note, for the calculation of the drag and lift coefficient uncertainty, it is assumed that only the uncertainty in the Z direction has a direct impact on the drag force, since it acts mainly in the same direction, while for the lift coefficient, only the uncertainties in the X and Y directions are used in the calculations. Thus, the results are 7% uncertainty on the drag coefficient, but it is up to 44% for the lift coefficient.

6. Results

The Reynolds number of the bubbles (Re_b) was in a range from about 400 to 650. In this range, a bubble freely rising in stagnant water exhibits oscillating motion along the rising path with shape change. The predicted shape is ellipsoidal, although not necessarily symmetric. Further, bubble/wall interaction induces a decrease in the lateral dimensions, and an increase in the vertical dimension. For $0.12 < \lambda < 0.6$ ($\lambda = d_e/D$, the wall effect factor), and $\mathrm{Re}_b > 100$, walls can cause elongation of bubbles in the vertical direction, so for the ellipsoidal bubble shape, the resulting shape would tend to change to spheroidal shape.

In this experiment, helical paths with rocking motion were observed. The wall effect factor was λ = 0.21, (Re_b >100 in all cases) so the wall influence was expected to be noticed. Therefore, by combining the effects of the contaminants and the interaction frequency with the pipe wall, the resulting bubble shape should be closer to a spheroid than an ellipsoid. Both the instantaneous and average values of the semiaxes showed that the bubbles' shape was oblate spheroidal for the whole range of Re_b. Figure 2 presents typical samples of shapes and trajectories obtained in the measurements.

6.1. Bubble dimensions, velocity and dimensionless parameters

Table I shows average values for the bubbles' semiaxes and a spherical-equivalent diameter determined from 3D reconstructions. Note, however, that the difference in the semiaxes' length is within the calculated experimental error. Table I also shows the average value for the bubble speed, which is the magnitude of the 3D velocity vector, from which the bubble Reynolds number was determined.

In an infinite medium, both Grace's shape map [20], and Bhaga and Weber's shape map [21] predict $\mathrm{Re}_b \approx 800$ for Eo = 1 and M = 2.56×10^{-11} (air-water system). If the data in Table I are taken as representative for the whole range, the average Re_b shown is about 35% lower. However, experimental data show that air bubbles have lower velocities when rising in contaminated water. By assuming the terminal velocity in an infinite medium, $U_{\mathrm{T}\infty}$, to be about 220 mm/s for an air bubble with d_e = 2.7 mm in tap water [3], thus Re_b = 594, which is still about 15% higher than the Re_b shown in Table I. To quantify the wall influence on bubble rise velocity, the following Eq. (1) is used:

$$\frac{U_{\mathrm{T}}}{U_{\mathrm{T}\infty}} = \left(1 - \lambda^2\right)^{3/2}. \tag{10}$$

Thus, U_{T} in this case decreased by about 7%, and thus Re_b = 552, which is about 7% higher than that in Table I. By considering that only average values, over the whole Re range of 250, were used in these calculations, plus the error associated with the measurements, the experimental data in this study agree reasonably with known theory and other data.

6.2. Bubble drag coefficient

Figure 3 shows the instantaneous drag coefficient values derived from measurements in this study as a function of Re. For comparison, approximate data from Haberman and Morton's report [3] are also included. Drag coefficient values were first computed using equivalent diameter, acceleration,

and velocity of individual bubbles in (9). Then, it was assumed that instantaneous velocities were already terminal velocities, since, as previously discussed, C_D values are frequently determined at this condition. In this case C_D can be computed from

$$C_{\mathrm{D}} = \frac{4}{3}\frac{d_e}{U_b^2}g. \tag{11}$$

Figure 3 shows that the C_D computed from (9) and the one obtained from (11) have practically the same trend and values, and the data converge at the upper boundary of the Re measurement range. Additionally, it can be noted in Fig. 3 that the C_D in Haberman and Morton's data for both tap and filtered water reaches a minimum at Re before 500, and then it increases its magnitude as Re increases. In the data from this experiment and the standard drag curve, however, C_D decreases as Re increases, although it does not appear to plateau for Re about 600. To explain this difference in behavior with fluid particles and the similarity with rigid particles, it has to be considered that PIV measurements require the addition of micrometer-size tracer particles to the continuous phase. Thus, accumulation of tracers on the bubble's surface leads this fluid particle to behave more like a rigid particle, which is known to exhibit boundary layer separation and vortex shedding at lower Re. Therefore, a "contaminated" bubble has higher C_D values than a "clean" fluid particle. Experimentally, it has also been proven that at Re lower than about 400 both rigid spheres and bubbles in tap water have practically the same C_D value, but bubbles in pure liquids delay their boundary layer separation, so their C_D is lower than bubbles in contaminated systems and rigid particles [3].

Note in Fig. 3 that for Re about 550, C_D reaches those values corresponding to bubbles freely rising in tap water, but there are no data in this experiment to figure out if it would continue on the same trend as a fluid particle. The difference in C_D magnitude below (about) 550, besides measurement error, is attributed to wall effect, as bubbles with Re higher than about 500 were rising primarily close to the pipe core. Those bubbles rising close to the pipe wall experience flow shear generated by flow acceleration around the bubble plus flow deceleration because of wall friction, which increases the bubble drag. For the instantaneous drag coefficient data in Fig. 3, the error was determined to be 7%, as explained before.

In a recent study, Pang and Wei [22] performed an analysis of different expressions to compute drag and lift coefficients for use bubbly flow computations. These authors concluded that the relationship best suited for the calculations of the drag coefficient is that one developed by Zhang and VanderHeyden [23]. Figure 4 shows a comparison of experimental data from this study and Haberman and Morton's report against values obtained by using the Zhang and VanderHeyden's expression. Since correlations are meant to provide average values, the data from our measurements have been averaged over Re bins with a width of 50, to perform a proper comparison. It can be noted that, when averaged, values from

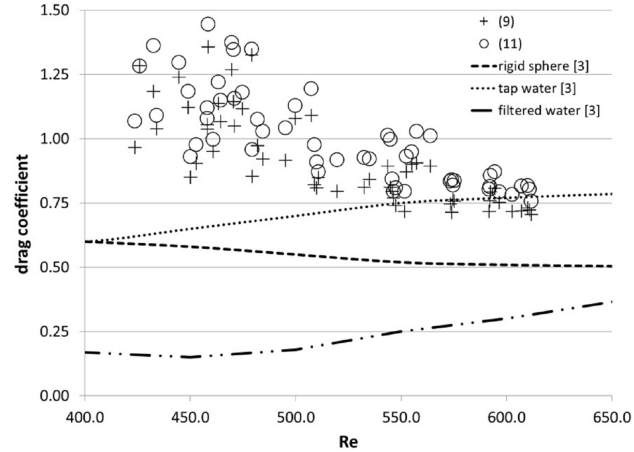

FIGURE 3. Comparison of instantaneous drag coefficient values obtained in this experiment, as a function of bubble Reynolds number, and Haberman and Morton's data.

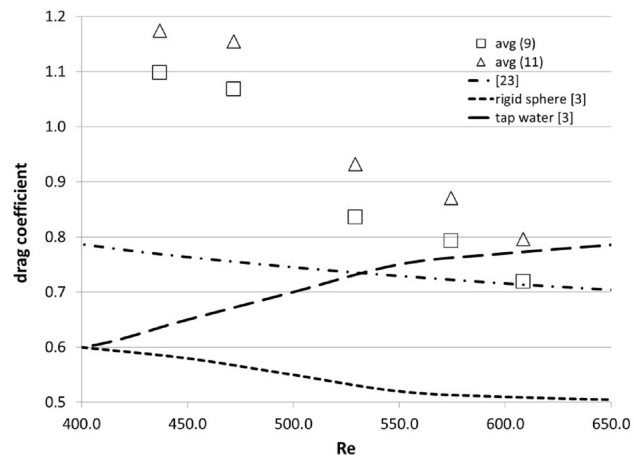

FIGURE 4. Comparison of bin-averaged values of drag coefficient as a function of bubble Reynolds number and data by Haberman and Morton, and Zhang and VanderHeyden's expression.

using the terminal velocity expression are about 10% higher on average.

Figure 4 also shows that measurements in this study and Zhang and VanderHeyden's expression have the same profile over the whole Re of interest, but C_D magnitudes differ quite significantly until Re of about 600, where the data tend to converge. The data from all 11 correlations shown by Pang and Wei have the same profile. By using (10) again and considering that a bubble close to the pipe wall moved within a zone of about 4 mm, the terminal velocity would decrease about 40%, which leads to a significant increase in C_D magnitude. Therefore, use of the correlations for determining the drag coefficient should consider wall influence, and take Re in a range from 500 to 550 as a threshold.

6.3. Bubble lift coefficient

Table I also shows the results obtained for the average lift coefficient. For instantaneous values, no clear trend was found for the data. The data points from this experiment were quite

scattered about an average value of 0.39. When bin-averaged, for Re above 500, instantaneous data values were close to 0.3, which is the value predicted by Tomiyama *et al.* [24]. For Re below 500, when bin-averaged, lift coefficient values were about 0.5. Pang and Wei suggest using the expression by Legendre and Magnaudet [25], which tends to a value of 0.5 in the Re range of interest. This value is also predicted by other theoretical and numerical studies for spherical particles in inviscid fluid. It is important to recall that the present lift coefficient measurements are considered to have an associated error of up to 44%. As in the case of the instantaneous drag coefficient data, Re in a range from 500 to 550 seems to be the threshold for wall influence, but due to the high uncertainty this range cannot be taken as reliable.

7. Conclusions

The combination of Particle Tracking Velocimetry and Shadow Image Velocimetry techniques has been used for a full-volume, three-dimensional, transient experimental study of single bubble dynamics in restricted media. This hybrid technique allowed for measurements of bubble shape, dimensions, orientation, trajectory, velocity, and acceleration of bubbles rising in stagnant tap water. These parameters were then used to compute the drag and lift forces acting on the bubble. Drag and lift coefficients were then determined. Both instantaneous and averaged data are presented in this study.

In this study, the bubble Reynolds number ranged from 400 to 650. The results show that the presence of tracers in the water had a significant influence on the dynamics of the air bubbles. The measurements showed that the instantaneous bubble drag coefficient profile, as a function of Re, is different from that of fluid particles, as indicated by a comparison with data from correlations and other experiments found in the scientific literature. The same profile is, however, similar to the trend of the standard drag curve for rigid spheres and to profiles obtained from bubble C_D correlations used frequently in bubbly flow computations. At Re about 600, the data from this experiment, data for tap water by Haberman and Morton, and Zhang and VanderHeyden's expression did tend to converge. Also, drag coefficient values calculated using the terminal velocity condition were about 10% higher than those computed through force balance, but both profiles are similar. In the Re range of measurements, those bubbles rising close to the pipe wall showed a significant difference in drag coefficient magnitude, when compared to data from correlations and other experiments in which the wall influence on bubble movement did not exist. Therefore, correlations intended for determining the drag coefficient values should be adequately modified to account for wall impact when necessary, since the drag coefficient magnitude is considerably higher than that predicted by such correlations at Re below a region of about 500 to 550. Regarding the lift coefficient, no clear tendency can be delineated as a function of bubble Reynolds number. When bin-averaged, lift coefficient values are about 0.5 at Re below 500, and 0.3 above that same Re. However, due to the high uncertainty these values are not reliable.

The major contributors to the uncertainty in this experiment were the capability of accurately reconstructing the 2D shape of the bubbles from distorted and/or incomplete PIV images and determining the bubble centroid. Uncertainty of both velocity and acceleration depend directly on the accuracy of the bubble's centroid calculation, and that uncertainty was reflected on the computation of the drag and lift forces. The uncertainty analysis showed that the lift coefficient values obtained in this experiment have up to 44% error. For the drag coefficient, the error associated with each instantaneous value was calculated to be 7%.

The present experimental study has also made apparent the need of obtaining high spatial resolution image data to compute accurate values of the lift force and coefficient. The time resolution is another issue. Even though the CCD cameras were run in field mode at 60 Hz, only 3 or 4 images of a rising bubble could be acquired, thus limiting the possibility of performing more reliable measurements of velocities and accelerations or volume changes. Nowadays, 1000×1000 pixels resolution and higher than 100 frames per second are standard features of CCD cameras, thus both spatial and temporal resolutions can be greatly increased. Moreover, higher spatial resolution allows using sub-pixel accuracy algorithms, which, in turn, can further improve measurement accuracy. It is considered that the uncertainty on the bubble's centroid coordinates must be less than 1 μm, in order to get uncertainties of lift coefficient calculations of about 10 to 15%. While it is clear that new technology has overcome these spatial and time resolution issues, the required 2D and 3D bubble shape reconstruction steps still need to be carried out. Therefore, the uncertainties associated to the reconstruction process and their contribution to the whole process of determining the values of drag and lift coefficients must be taken into account.

1. R. Clift, J.R. Grace, and M.E. Weber, *Bubbles, Drops and Particles* (Academic Press, New York, NY, 1978).
2. L.S. Fan and K. Tsuchiya, *Bubble Wake Dynamics in Liquids and Liquid-Solid Suspensions* (Butterworth-Heinemann, Stoneham, MA, 1990).
3. W.L. Haberman and R.K. Morton, *An Experimental Investigation of the Drag and Shape of Air Bubbles Rising in Various Liquids* (Report 802, NS 715-102, 1953).
4. Z. Lanying, S. Balachandar, P. Fischer, and F. Najjar, *J. Fluid Mech.* **37** (2008) 271.

5. E.E. Michaelides, *J. Fluids Eng.* **119** (1997) 233.
6. F. Takemura, S. Takagi, J. Magnaudet, and Y. Matsumoto, *J. Fluid Mech. 461* (2002) 277.
7. C. Crowe, M. Sommerfeld, and Y. Tsuji, *Multiphase Flows with Droplets and Particles* (CRC Press, Boca Raton, FL, 1998).
8. W.C. Park, J.F. Klausner, and R. Mei, *Experiments in Fluids* **19** (1995) 167.
9. C.E. Brennen, *Cavitation and Bubble Dynamics* (Oxford University Press, New York, NY, 1995).
10. J.R.C. Hunt, R.J. Perkins, and J.C.H. Fung, *Review of the Problems of Modeling Disperse Two-Phase Flows*. Multiphase Science and Technology. Volume 8 Two-Phase Flow Fundamentals. Editors G.F. Hewitt, J.H. Kim, R.T. Lahey, Jr., J.M. Delhaye, and N. Zuber, (Begell House, New York, NY, 1994) 595.
11. J. Magnaudet, M. Rivero, and J. Fabre, *J. Fluid Mech.* **284** (1995) 97.
12. F. Takemura and J. Magnaudet, *J. Fluid Mech.* **461** (2003) 277.
13. Y. Hardalupas, K. Hishida, M. Maeda, H. Morikita, A.M.K.P. Taylor, and J.H. Whitelaw, *Applied Optics* **33** (1994) 8147.
14. S.M. Hwang, R. Kurose, F. Akamatsu, H. Tsuji, H. Makino, and M. Katsuki, *Energy & Fuels* **19** (2005) 382.
15. G.T. Marzan and H.M. Karara, *Proc. of the Symposium on Close-Range Photogrammetric Systems* (1975) 420.
16. K. Okamoto, Y. A. Hassan, and W.D. Schmidl, *Exp. Fluids* **19** (1995) 342.
17. Y.A. Hassan and O.G. Philip, *Exp. Fluids* **23** (1997) 145.
18. N. Ayache, *Artificial Vision for Mobile Robots: Stereo Vision and Multisensory Perception* (The MIT Press, Cambridge, MA. 1991).
19. J. Ortiz-Villafuerte, Y.A. Hassan, and W.D. Schmidl, *Exp. Thermal Fluid Sci.* **25** (2001) 43.
20. J.R. Grace, T. Wairegi, and T. H. Nguyen, *Trans. Inst. Chem. Eng.* **54** (1976) 167.
21. D. Bhaga and M.E. Weber, *J. Fluid Mech.* **105** (1981) 61.
22. M.J. Pang and J.J. Wei, *Nuclear Eng. Design* **241** (2011) 2204.
23. D.Z. Zhang and W.B. VanderHeyden, *Int. J. Multiphase Flow* **28** (2002) 805.
24. A. Tomiyama, H. Tamai, I. Zun, and S. Hosokawa, *Chem. Eng. Sci.* **57** (2002) 1849.
25. D. Legendre and J. Magnaudet, *J. Fluid Mech.* **368** (1998) 81.